Quantification of the impact of acidified brine on fracture-matrix transport in a naturally fractured shale using in situ imaging and modeling

Christopher Zahasky[a,1], Manju Pharkavi Murugesu[b], Takeshi Kurotori[b], Collin Sutton[a], Jennifer L. Druhan[c], Bolivia Vega[b], Sally M. Benson[b], Anthony R. Kovscek[b]

[a] *Department of Geoscience University of Wisconsin-Madison Madison WI 53706 United States*
[b] *Department of Energy Resources Engineering Stanford University Stanford CA 94305 United States*
[c] *Department of Geology University of Illinois at Urbana-Champaign Urbana IL 61801 United States*

Abstract

Understanding flow, transport, chemical reactions, and hydro-mechanical processes in fractured geologic materials is key for optimizing a range of subsurface processes including carbon dioxide and hydrogen storage, unconventional energy resource extraction, and geothermal energy recovery. Flow and transport processes in naturally fractured shale rocks have been challenging to characterize due to experimental complexity and the multiscale nature of quantifying exchange between micrometer-scale fractures and nanometer-scale pores. In this study, we use positron emission tomography (PET) to image the transport of a conservative tracer in a naturally fractured Wolfcamp shale core before and after exposure of the core to low pH brine conditions. Image-based experimental observations are interpreted by fitting an analytical transport model to every fracture-containing voxel in the core. Results of this analysis indicate subtle increases in matrix diffusivity and a strong reduction in fracture dispersivity following exposure to low pH conditions. These observations are supported by a multi-component reactive transport model that indicates the capacity for a 10% increase in porosity at the fracture-matrix interface over the duration of the low pH brine injection experiment. This porosity enhancement is the result

of exposure of carbonate minerals in the shale matrix to low pH conditions. This workflow represents a new direct approach for quantifying fracture-matrix transport processes and provides a foundation for future work to better understand the role of coupled transport, reaction, and mechanical processes in naturally fractured rocks.

Keywords: shale, fractures, X-ray computed tomography, positron emission tomography, reactive transport, models

---

1. Introduction

A quantitative and predictive understanding of transport across fracture-matrix interfaces in shale formations is vital to the management and engineering of a range of flow and transport processes. These processes include groundwater protection from infiltrating contaminants [1], storage security of geologically sequestered CO_2 [2, 3, 4], resource recovery following hydraulic fracturing [5, 6, 7], and long-term nuclear waste storage security [8, 9].

Flow and transport processes between fractures and matrix/host rock material have been quantitatively described with a range of numerical and analytical modeling approaches. Large fracture networks have been modeled with multiple interacting continua approaches (e.g. dual porosity, dual permeability) [10, 11, 12, 13], or large discrete fracture networks where the fractures are explicitly defined [14, 15]. Simulation of flow in a small number of fractures can be accomplished using explicit flow field modeling by solving the Navier-Stokes equation when fracture geometry can be constrained or approximated [16, 17], or using hybrid or micro-continuum approaches [18].

In addition to numerical approaches, analytical models have been derived to describe solute transport in fractured systems. Describing solute transport into matrix material with analytical models often relies on the assumption that the matrix can be considered infinite and the concentration of solute in the fracture is constant [19, 20]. A more sophisticated solution was derived that can also account for advection and dispersion in the fracture [21]. Semi-analytical

solutions have been expanded to solve for these processes in two dimensions along a single fracture [22]. The advantage of these analytical methods is that they can be readily applied to solve for transport parameters within simple systems or sub-domains (i.e. voxels) within more complex systems.

A key barrier to predictive understanding of transport between fracture and matrix in many geologic settings is quantifying these processes in response to changing fluid chemistry conditions. In many contexts, the overprinting of natural environmental conditions by anthropogenic activities results in transient variations in pore fluid chemistry which can drive a range of precipitation and dissolution reactions that alter fracture-matrix transport behavior [23]. Mineralogical composition of shale rocks is often categorized into the proportion of shale matrix composed of carbonate minerals (e.g. calcite and dolomite), silicates (e.g. quartz, feldspars, and pyrite), and clays (e.g. illite and smectite) [6]. In the presence of complex brines and when subject to rapid shifts in pH and solute chemistry, this multicomponent, multispecies system presents a highly coupled, non-linear reactive transport problem [24] requiring numerical reactive transport models to track and predict behavior [25, 26, 27, 28, 29, 24, 30, 31].

Multiscale quantification of flow, transport, and reactions is often complicated by uncertainty about the applicability of experimental batch measurements under ambient conditions to larger-scale dynamic system behavior [32]. In cases where flow-through experiments are performed under elevated pressure and temperature, typically only one measurement may be possible in a given sample [33]. X-ray computed tomography (X-ray CT) is a key tool used to recover three-dimensional information about fracture geometry and multiphase flow under in situ conditions in geologic materials [34, 35, 4]. However, quantification of solute transport can be challenging with X-ray CT due to the need to use high photon attenuating tracers. These tracers can create gravitational artifacts and have very low signal-to-noise ratios as solute concentration decreases. These challenges are amplified in samples with micron-scale fracture apertures [36, 37, 38].

Positron emission tomography (PET) is a complementary in situ imaging

technique that relies on the injection, detection, and reconstruction of high-energy photons from positron-emitting radiotracers. Tomographic reconstruction methods are used to acquire three-dimensional time-lapse images of radiolabeled compound distribution in geologic materials. This three-dimensional imaging provides thousands of concentration measurements as a function of time throughout a sample, enabling multiscale transport quantification. The 511 keV photons emitted during positron emission and annihilation events are ideally suited for geologic materials that otherwise cause significant photoelectric adsorption and attenuation of lower energy photons [37]. This technique has recently been used to quantify solute advection and dispersion in highly heterogeneous sandstones under saturated and unsaturated flow [39, 40, 41] and to quantify absorption in microporous carbonates [42].

In this study, we employ PET imaging to provide the unprecedented quantification of spatially variable fracture-matrix transport associated with natural fractures in a Wolfcamp formation shale sample before and after acidic reactive fluid injection. Slug radiotracer injection with simultaneous PET imaging is performed and an analytical solution to the advection-dispersion equation is used to interpret voxel-scale fracture-matrix transport. A weak acidified brine injection (pH=4) was then performed for 21 days followed by a repeated slug tracer imaging experiment. This second post-acid experiment enabled the quantification of changes in transport behavior resulting from extended exposure to low pH conditions. A multi-component numerical reactive transport model (RTM) is constructed to confirm the extent of reactive alteration based on acid-neutralizing solubilization of carbonate minerals at the fracture-matrix interface. The RTM offers independent verification of the interpretation of experimentally-observed changes in fracture-matrix transport behavior.

2. Methods

2.1. Sample characterization and brine fluid chemistry

The core used is a cylindrical Wolfcamp shale core with a diameter of 25 mm and a length of 58 mm acquired from the Permian Basin at a depth of 2867 m. Mineral composition and organic content of the core were measured using X-ray diffraction analysis and source rock analysis respectively. Both measurements were conducted by Core Laboratories. Core mineralogy and organic characteristics are shown in Table A.3 and were reported in previous studies [43]. Synthetic brine was created following the Wolfcamp brine recipe (Table 1) that was previously developed to establish chemical equilibrium with Wolfcamp shale, thus minimizing reactivity prior to the acidification experiment [31].

Table 1: Composition of synthetic brine solution.

Composition	Potassium Chloride	Calcium Chloride	Magnesium Chloride	Sodium Chloride	Sodium Nitrate	Sodium Sulphate	Sodium Bicarbonate
wt%	1.1	5.23	1.49	90.9	0.06	0.80	0.39

2.2. Experimental CT data acquisition

The Wolfcamp core sample was first dried for 120 hours in a vacuum oven at 45°C until the sample mass stabilized. The core was sealed between the coreholder inlet and outlet end caps using high-strength heat-shrink fluorinated ethylene propylene tubing. The core was then wrapped with an aluminum foil to provide a gas diffusion barrier [44, 40]. The coreholder inlet and outlet end caps had flow channels connecting to the core with dead volumes of 0.58 cm^3 and 0.98 cm^3, respectively. The core with end caps were fit into a high-pressure aluminum coreholder that enables the application of confining pressure using tap water as the confining fluid. The seal around the core was pressure-tested for 24 hours to ensure complete isolation of pore fluids from the confining fluid.

Prior to pore fluid injection, a confining pressure of 1720 kPa (250 psi) was applied and the sample was vacuumed using a vacuum pump (*Leybold D16B*,

ultimate pressure: 1×10^{-4} mbar). With the vacuum applied, the sample was imaged daily using an X-ray CT scanner (*GE LightSpeed*) operated at 140 kV and 120 mA with an exposure of 1 second per scan. The raw voxel size was $195\times195\times625$ µm^3 and the field of view of was 10 cm. Complete vacuum was reached when the CT number in Hounsfield units of the core ceased to decrease further. The core was then saturated with krypton gas (99.999% purity) at 2068 kPa (300 psi) and confining pressure of 3790 kPa (550 psi). Krypton has a large X-ray attenuation coefficient and fills the pore space of the core with inert gas allowing the porosity (ϕ) of the core to be quantified via linear scaling [35]. The core was then vacuumed again and saturated with CO_2 (100% purity) at 2068 kPa (300 psi) before injecting the prepared synthetic brine solution described in Table 1. The brine was injected at a pressure of 3650 kPa (530 psi) with a backpressure of 3170 kPa (460 psi) and confining pressure of 4826 kPa (700 psi). Pyrite oxidation was minimized by purging nitrogen gas through the injected brine used in all experiments to displace any dissolved oxygen. All pressure conditions were controlled by high-pressure syringe pumps (*Teledyne ISCO*). The brine imbibition process was monitored and the core was determined to be fully saturated based on X-ray CT scans [43].

2.3. Experimental positron emission tomography data acquisition

Two sets of tracer experiments imaged with PET were performed, one before low-pH brine injection and one after the low-pH brine injection as described in the following section. PET imaging experiments were performed with an experimental platform specifically designed for the safe injection, quantification, and disposal of radiotracers with simultaneous in situ PET imaging. Continuous aqueous phase injection was achieved with a *Vindum VP-3K* dual piston pump plumbed to a 1000 mL *Parker* piston accumulator filled with the brine mixture described in Table 1. The fluid injection rate for both PET imaging experiments was 0.01 mL/min and pore pressure conditions throughout both experiments were approximately 2000 kPa (290 psi). A second *Vindum VP-6K* dual piston pump applied a confining pressure to the core of 3790 kPa (550 psi).

The positron-emitting radiotracer [^{18}F]-fluorodeoxyglucose (FDG) was used for the imaging experiments. This commercially available radiotracer has a half-life of 109.7 minutes and has been found to behave as an ideal tracer in a range of geologic materials in part because of the charge neutrality of FDG. Fluorodeoxyglucose was diluted in 3 mL of the brine described in Table 1 to reach the optimal radioactivity concentration for minimizing imaging noise [37]. Precise control of the radiotracer injection and timing was controlled using a six-port dual-position *VICI Cheminert* HPLC rotary valve with a 3 mL injection loop. Pressure and radiation sensors enabled continuous measurement of fluid pressure, pump pressures, and injected radiotracer concentration. To safely handle radioactive liquids, the experimental system utilized extensive lead shielding around the radiation sources.

The PET scans were performed using a *Siemens Inveon DPET* pre-clinical scanner at the University of Wisconsin-Madison small animal imaging and radiotherapy facility (SAIRF). Each experiment was completed in 12 hours with four three-hour scans. Due to the length of the experiment, the image timesteps were discretized into 5-minute intervals. However, PET imaging enables timesteps as short as 20 seconds to monitor more rapid transport processes [37]. Sequential PET scans were concatenated together in time by decay correcting to the scan start time [38]. Confirmation of tracer mass balance after image concatenation is illustrated in Figure B.8 in Appendix B. Additional details and theoretical background related to PET imaging experiments in geologic materials are described in previous work [37].

2.4. Low-pH brine injection experimental procedure

Following the first PET scan, the core was exposed to continuous flow-through of pH 4.0 brine analogous to conditions that might occur when brine is saturated with dissolved CO_2. To perform this experiment, the core was again connected to a pump containing the synthetic brine mixture described in Table 1. The experimental setup is similar to that described in Section 2.2 but adapted for the more acidic brine injection [45]. Brine was injected through the core for

a period of seven days to ensure the displacement of any remaining FDG in the core. The injection line of the core was then connected to a piston accumulator (*Parker A3NW0058D1E* with a nickel coating) containing the brine solution with the addition of hydrochloric acid (*Baker Analyzed*, assay: 37.1%, density: 2.7 kg/1 L). This produced a brine solution with a pH of 4.0 that was then injected continuously at a pressure of 2200 kPa (320 psi), backpressure of 1510 kPa (220 psi) and confining pressure of 3790 kPa (550 psi) for 21 days. The reacted brine was produced at the outlet. At these conditions a total of 55.4 pore volumes of weakly acidic brine was injected over the 21 day period.

Throughout the pH 4.0 brine injection the core sleeve was covered with heat tape and insulated to maintain a constant temperature of 40 °C. This temperature regulation was principally employed to more closely represent in situ reservoir conditions. Following the 21 day injection, a second conservative tracer PET scan was performed under identical conditions as the first PET experiment as described in Section 2.3.

2.5. Fracture identification and PET image processing

To quantify fracture-matrix transport, the raw PET scans were segmented into voxels containing fractures and voxels not containing fractures. The raw data was first coarsened by a factor of two, giving a voxel size of 1.6 mm×1.6 mm×1.6 mm. Raw images were coarsened by a factor of two by taking the arithmetic average of 2×2×2 voxels, thereby also reducing the number of voxels by a factor of 8. Coarsening was performed to reduce imaging noise [37] and to ensure that the voxels with fractures had a large matrix-to-fracture ratio. This voxel size enables the approximation that voxel-average concentration changes were diffusion dominated and that the quantity of the tracer in the fracture could be neglected from analytical model fitting. The radiotracer in the fracture is assumed to be negligible because the fracture apertures were estimated to be in the tens of micrometers based on the X-ray CT images and therefore occupied less than one percent of the coarsened voxel volume. Fractures were located by first applying the Frangi vesselness filter [46]. The Frangi filter has been

used to detect image features such as vessels, wrinkles, and rivers [47, 48]. Filtered images were then thresholded to select voxels in the core that most likely correspond to voxels containing fractures.

2.6. Semi-analytical fracture matrix transport model description

Once voxels containing fractures were identified from the PET images, an analytical transport model was fit to each voxel breakthrough curve. An analytical solution was employed that accounts for advection and dispersion along the fracture and diffusion into the matrix [21]. Fitting the analytical solution to each voxel breakthrough curve enabled the voxel-scale estimation of matrix tortuosity (τ'), local fracture longitudinal dispersivity (α_z), and local fracture advection velocity (v_z).

The differential equation for solute transport in the fracture is given by

$$\frac{\partial C}{\partial t} - D_z \frac{\partial^2 C}{\partial z^2} + v_z \frac{\partial C}{\partial z} + \frac{q}{b} = 0 \tag{1}$$

Here, D_z is the hydrodynamic dispersion coefficient in the fracture that can be defined by $D_z = \alpha_z v_z + \mathcal{D}$ where $\mathcal{D}$ is the bulk molecular diffusion coefficient in water. A value of molecular diffusion of $\mathcal{D}$ =6.7e-6 [cm^2/s] was assumed based on the diffusion coefficient of glucose in water. The variable q is the diffusive flux perpendicular to the fracture face and b is half of the fracture aperture. The mean fracture aperture was estimated to be 20 μm using the calibration free missing attenuation method [38] on the X-ray CT scan shown in Figure 1.

Advection in the matrix is assumed to be negligible so that transport can be described by the diffusion equation.

$$\frac{\partial C'}{\partial t} - D' \frac{\partial^2 C'}{\partial x^2} = 0 \tag{2}$$

The notation C' explicitly denotes the concentration of solute in solution in the matrix following the original notation of Tang et al [21]. The variable D' is the effective diffusion coefficient in the matrix that is defined as $D' = \tau' \mathcal{D}$ where τ' is the matrix tortuosity as defined in [49] and [21]. Note that this is related to the more common definition of tortuosity (τ) as the distance some particle

must travel through a porous media relative to the straight line distance. These two definitions of tortuosity are related by the expression $\tau' = \phi/\tau$ [50, 51].

The solution for matrix concentration (C') at a distance (z) from the inlet of the core, a distance (x) from the center of the fracture as a function time t has been previously derived [21]. Specifically, for the following boundary and initial conditions

$$C'(b, z, t) = C(z, t) \tag{3}$$

$$C'(\infty, z, t) = 0 \tag{4}$$

$$C'(x, z, 0) = 0 \tag{5}$$

the solution for matrix concentration (C') based on the coupled Equations 1 and 2 is given by Equation 6.

$$\frac{C'}{C_0} = \frac{\exp(\nu z)}{\pi^{1/2}} \int_l^\infty 2 \exp\left[-\xi^2 - \frac{\nu^2 z^2}{4\xi^2}\right] \exp(-\eta z^2) \mathrm{erfc}\left[\frac{Y'}{2T}\right] d\xi \tag{6}$$

Here T and Y' are given by Equation 7 and 8, respectively.

$$T = \sqrt{t - \frac{z^2}{4D\xi^2}} \tag{7}$$

$$Y' = \frac{v^2 \beta^2 z^2}{4A\xi^2} + B(x - b) \tag{8}$$

Variables ν and β are defined as $\nu = v/2D$ and $\beta = \sqrt{4D/v^2}$. The lower limit of the integral (l) in Equation 6 is equal to Equation 9.

$$l = \frac{z}{2} (Dt)^{-1/2} \tag{9}$$

Note that unlike the original solution of Tang et al [21], the first-order reaction/decay terms are neglected because all of the reconstructed PET data are decay corrected based on the 109.7 min half-life of ^{18}F.

Equation 6 was solved with a two-step composite trapezoidal function programmed in Python. The first step was to determine the upper limit of the integral in Equation 6—below which the integrand is greater than zero. The second step was to then solve the integral between l and this upper limit with

a very fine discretization of ξ. This two-step numerical method was found to be more numerically efficient than the Gaussian quadrature method. To fit this equation to the volume-average concentrations in each fracture-containing voxel as a function of time, Equation 2 was solved as a function of distance into the matrix (x) at each timeframe. This resulted in a concentration profile as a function of distance x from the fracture center to the voxel edge—assuming the fracture was in the middle of the voxel. This profile was then integrated as a function of x to calculate the total amount of radiotracer in a the voxel at a given time. To fit the analytical model to the measured breakthrough data, a non-linear least squares fitting routine was developed using SciPy package functions. The processed data and Python codes used for analysis and analytical modeling are available in the data repository cited in the Acknowledgements.

2.7. One-dimensional reactive transport simulation

A multi-component RTM was developed to quantify the extent of fracture-matrix alteration during low pH fluid injection and independently verify the extent of alteration suggested by the experimental results and fracture-matrix transport model. A one-dimensional (1D) RTM was constructed in the open-source numerical reactive transport software CrunchFlow [29]. The RTM tracks changes in mineral volumes resulting from solubilization due to exposure of the through-flowing weakly acidic brine. Initial condition mineral volumes used for the RTM were assigned based on mineral densities and the weight composition of the core (Table 2). The starting mineralogy includes plagioclase, specifically albite, and clays including smectite and illite. The injected fluid chemistry composition is based on the laboratory brine described in Table 1. Mineral reaction kinetics, temperature-dependent equilibrium coefficients, and multi-component aqueous speciation including the carbonate equilibria and associated feedbacks to pH, as shown in Table C.4 and C.5, are all included in the model based on prior Wolfcamp RTM simulations [5, 6, 7].

The model domain was oriented to allow transport perpendicular to the plane of the fracture with one end of the model representing the fracture-matrix

interface and the other end representing the no-flow walls of the core. The length of the model was 12.6 millimeters long and 1 millimeter wide. The bulk diffusion of HCl in water is $\mathcal{D}$ = 5.25e-5 cm^2/sec [52]. To set the model diffusion, the bulk diffusion was multiplied by $\tau' = 0.0125$ as approximated from the tortuosity determined in the first PET scan (described in the following section). The pressure drop from the fracture into the matrix was assumed to be low and was set to 6.9 kPa (1 psi). The temperature was set to 40 °C. The permeability of the matrix was approximated as 10 μD as estimated based on steady-state differential pressure following core saturation with brine. The starting porosity of the model was 10.2 percent as measured with the X-ray CT scan and identical to the value used for the analytical transport model. The model input files and database are available in the data repository cited in the Acknowledgements.

Table 2: Starting mineral volume fractions of the Wolfcamp sample specified in the reactive transport simulation.

Mineral	Quartz	K-Feldspar	Albite	Calcite	Dolomite	Pyrite	Illite	Smectite
vol%	57	1	4	0	3	1	22	1

3. Results

3.1. Fracture identification and concentration quantification with PET imaging

The core and fracture geometry are illustrated in the X-ray CT scan in Figure 1. The CT scan depicts one nearly through-going bedding-parallel fracture that intersects the inlet face of the core. There are several other small microfractures semi-parallel to this main fracture, including several that intersect the outlet face of the core. The results of the radiotracer injection and imaging with PET prior to acid exposure are illustrated in Figure 2. The red shading indicates radiotracer concentration in uncoarsened PET images in different slices along the axis of the core. The PET images clearly show the transport of tracer through these fractures identified in the X-ray CT scan.

Radiotracer injection and imaging before and after acid exposure are shown in Figures 2 and 3, respectively. Results of the coarsened and thresholded voxels containing fractures are highlighted by the grey shading in Figure 2 (pre-acid injection) and Figure 3 (post-acid injection). The threshold was selected such that there was a very high degree of confidence that the voxel contained the fracture and was not influenced by core boundary conditions. As a result, many voxels that likely contained fractures were neglected from the analytical parameter fitting. Regardless of these neglected voxels, there were 445 voxels thresholded in the pre-acid scan and 442 voxels thresholded in the post-acid scan. Note that while many of these voxels were in identical locations as can be seen by comparing Figures 2 and 3, the thresholding workflow did not include a routine to select identical sets of fracture-containing voxels due to subtle differences in image registration between the scans.

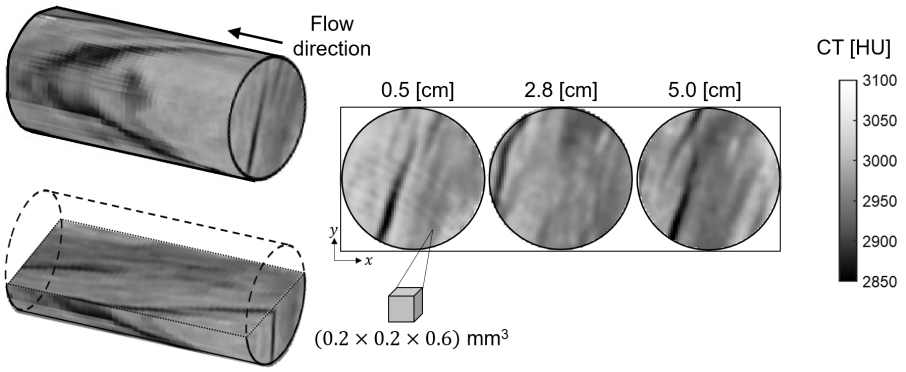

Figure 1: X-ray CT image of the Wolfcamp shale core. The two-dimensional slices illustrated on the right highlight the geometry of the fracture (darker regions) prior to low-pH fluid injection. The slices are taken at increasing distances from the inlet (z=0). The grey colorscale in all images is in Hounsfield units [HU].

3.2. Voxel-scale transport parameterization

Figures 4 and 5 show the results of fitting the analytical model (right plots) to the fracture-containing voxel breakthrough curves (left plots) before and after low-pH brine injection, respectively. The initial breakthrough of tracer in

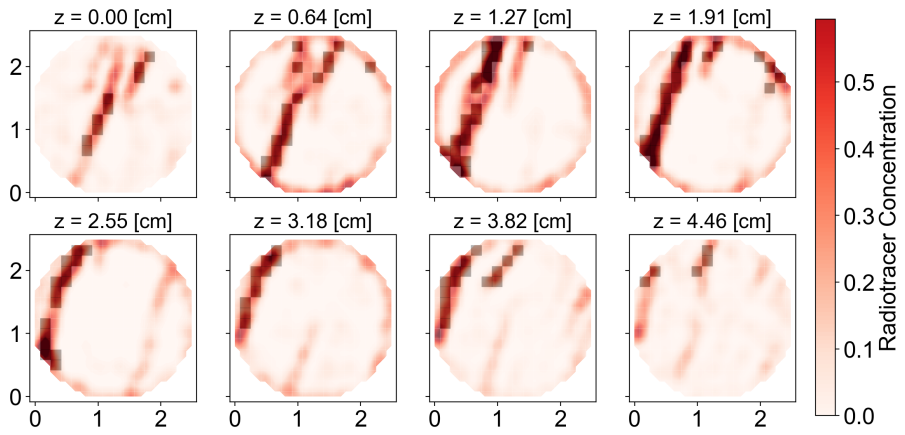

Figure 2: Two-dimensional slices through the core in the PET scan prior to acid exposure after 144 minutes of tracer injection. The slices are at increasing distance from the inlet (z=0). X and Y axes are length scales in centimeters. The red colorscale illustrates the radiotracer concentration and the shaded grey boxes highlight the thresholded voxels used for fitting the analytical transport model.

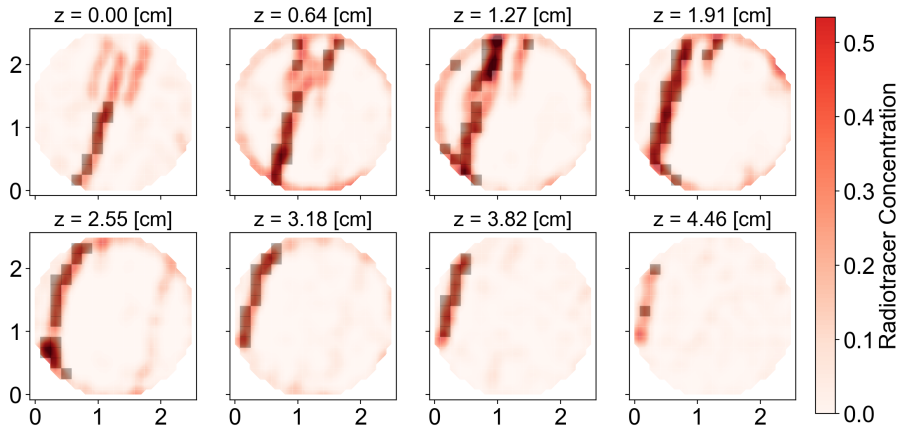

Figure 3: Two-dimensional slices through the core in the PET scan after acid exposure after 143 minutes of tracer injection. The slices are at increasing distance from the inlet (z=0). X and Y axes are length scales in centimeters. The red colorscale gives radiotracer concentration and the shaded grey boxes highlight the coarsened thresholded voxels used for fitting the analytical transport model.

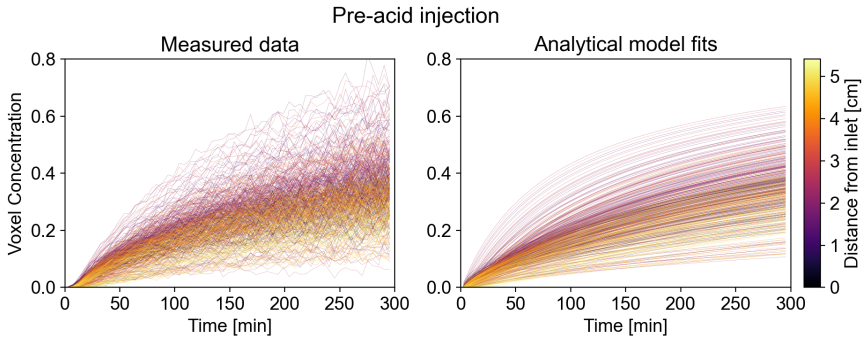

Figure 4: (left) Breakthrough curves for every voxel in the fracture determined from the PET scan prior to low-pH brine injection, as determined from the Frangi filter segmentation method described in Section 2.5. (right) Corresponding analytical fits to each voxel breakthrough curve. The colors in the analytical fit correspond to the same color of each voxel of measured data. The line color corresponds to the approximate distance from the inlet of the core in centimeters as described by the colorbar.

different voxels varied as a function of position along the length of the fracture. The line colors in Figures 4 and 5 are based on voxel distance from the inlet of the core. In all voxels the matrix tortuosity, fracture dispersivity, and fracture advection velocity were determined by fitting the analytical model to the breakthrough curves in the voxels containing fractures. It is clear from these figures that the analytical model was able to capture the measured concentrations despite the simplifying assumptions of the analytical model.

Statistical distributions of the fit parameters from the tracer tests before and after low-pH brine injection are illustrated in the histograms in Figure 6. The histogram of tortuosity values indicates that there is a slight shift toward higher matrix tortuosity and therefore matrix diffusion following low-pH brine injection. The dispersivity of the fracture is notably lower following acid exposure and the fracture advection velocity shows no systematic change following low-pH brine injection.

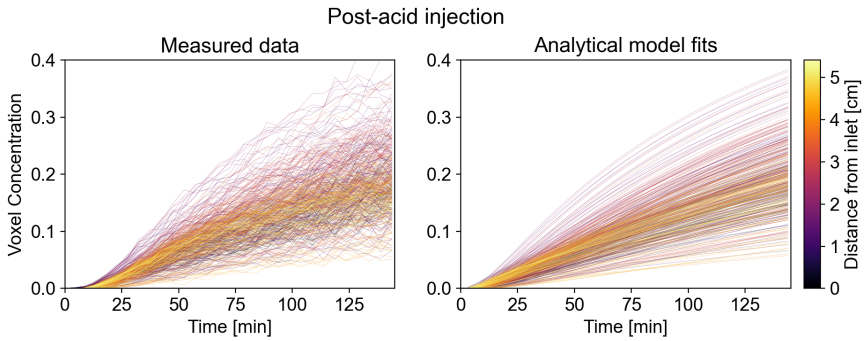

Figure 5: (left) Breakthrough curves for every voxel measured in the fracture using the PET scan taken after low-pH brine injection. (right) Corresponding analytical fits to each voxel breakthrough curve. The colors in the analytical fit correspond to the same color of each voxel of measured data. The line color corresponds to the approximate distance from the inlet of the core in centimeters as indicated by the colorbar.

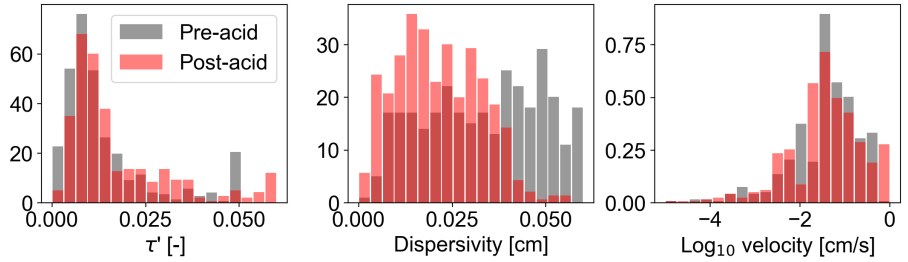

Figure 6: Histogram of fit tortuosity values (left) describing matrix diffusion, fracture dispersivity (center), and fracture advection velocity (left) before and after low-pH brine injection—indicated by grey and red shading, respectively.

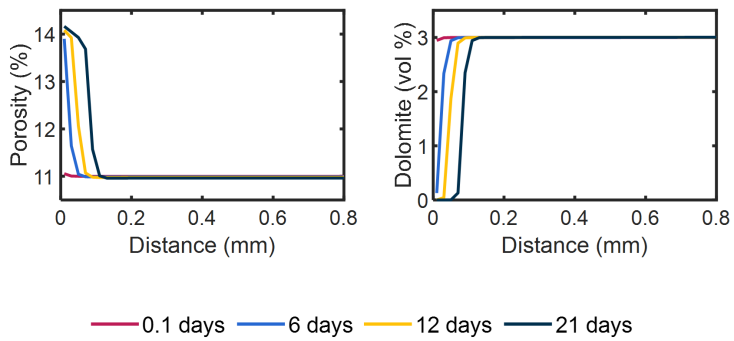

Figure 7: (Left) Model results of predicted porosity increase as a function of distance perpendicular to the fracture-matrix interface over a period of 21 days. (Right) Model output describing the reduction in dolomite volume in the matrix at increasing distance from the fracture-matrix interface due to dissolution.

3.3. One-dimensional reactive transport simulations of acidified fluid injection

The results of the 1D reactive transport simulation described in Section 2.7 are illustrated in Figure 7. Transport of reactive species within the matrix is almost entirely driven by diffusion. The results illustrate increasing porosity at the fracture-matrix interface caused by the rapid dissolution of dolomite as a function of injection time. Due to the reactivity of carbonate minerals, the dissolution front only progresses away from the fracture after all dolomite minerals have been dissolved. While these carbonates are still present, the acid is neutralized and reactivity is arrested. If reactive fluid injection was conducted for a longer period of time or with lower pH-brine, dissolution of additional minerals such as K-feldpsar, albite, smectite, and pyrite would lead to further porosity reduction over longer timescales as illustrated by the small volume changes of these minerals in the plots in Appendix C. As noted in Section 2.1, pyrite oxidation is assumed to be minimal because the sample was vacuumed and purged with CO_2 prior to saturating with brine that was purged with nitrogen gas prior to injection.

4. Discussion

The workflow of PET imaging, fracture-containing-voxel segmentation, and analytical model fitting demonstrates the first direct approach for millimeter-scale quantification of solute transport throughout a centimeter-scale shale core sample. This provides new insights into the distribution of parameters associated with transport through complex fracture geometry and diffusion into a spatially heterogeneous matrix. While a number of analytical solutions exist for describing the extent of fracture-matrix transport, the solution of Tang et al [21] is most applicable to the estimation of transport in the naturally fractured shale sample where advection in the matrix can be assumed to be negligible and the solute concentration in the fracture can not be assumed to be constant. Other analytical models could be substituted into this workflow based on the extent of matrix advection or differences in experimental boundary conditions or initial conditions. For example, future experiments may be able to utilize longer half-life radioisotopes such as ^{64}Cu that could be injected for a longer period of time to reach constant solute concentration conditions throughout a fractured core.

The reactive transport simulations independently support the experimental image-based observations, suggesting that acid exposure enhanced the connectivity of matrix pores near the fracture-matrix interface. Specifically, the dissolution of dolomite in the matrix shown in the right plot of Figure 7 corresponds to a subtle increase in porosity shown in the left plot of Figure 7 at the fracture-matrix interface. This dissolution is consistent with the slight increase in the matrix tortuosity factors following acid exposure as shown in the left plot in Figure 6. The increase in matrix tortuosity results in higher effective matrix diffusion.

In addition to enhanced connectivity, previous studies have shown that extended matrix exposure to acidic pH conditions results in shale softening [53, 54, 6]. Low pH conditions drive reactions in mineralogically heterogeneous shales that have been observed to increase surface roughness, drive fines migra-

tion, and induce clay swelling [6]. Our observations of an approximately linear permeability reduction from 15 μD to 7 μD over the course of the 21 day pH 4.0 brine injection experiment, combined with the reduction in fracture dispersion after low-pH brine injection shown in Figure 6, suggest reduced flow channelization and softening at the fracture-matrix interface. It is also possible that there was some mechanical deformation to fracture asperities due to pressurizing and depressurizing the confining pressure on the core during transport between imaging facilities.

5. Conclusion

In this study, slug tracer experiments were performed in naturally fractured Wolfcamp shale core and imaged with positron emission tomography before and after 21 days of injection of a low pH brine. Imaging results were used to quantify fracture-matrix transport by fitting a solution to the advection-dispersion equation [21]. This image-based transport quantification enabled the local voxel-level determination of matrix tortuosity, fracture dispersivity, and local advection velocity throughout the core sample. Distributions of local tortuosity and fracture dispersivity, combined with 1D reactive transport simulations, indicate enhanced diffusivity and shale softening at the fracture-matrix interface. This shale softening and reduced channelization led to lower permeability and reduced fracture channelization following exposure to low pH conditions.

The experimental imaging workflow and transport parameterization demonstrated in this study provides a new approach for understanding the spatial and temporal evolution of flow and transport behavior in naturally fractured core samples. These multiscale observations and models improve mechanistic understanding and scale translation of flow and reactive transport processes in shale formations in response to transient changes in pore fluid chemistry. This understanding is key for the management of groundwater resources, storage security of geologically sequestered CO_2, resource recovery following hydraulic

fracturing, and long-term nuclear waste repository design.

Acknowledgements

Datasets and analytical modeling and analysis codes are available at the Stanford Data Repository [55]. The experimental system used for column and imaging experiments was supported by the National Science Foundation under Grant No. 2002412. Any opinions, findings, and conclusions or recommendations expressed in this material are those of the authors and do not necessarily reflect the views of the National Science Foundation. This work was supported as part of the Center for Mechanistic Control of Unconventional Formations (CMC-UF), an Energy Frontier Research Center funded by the U.S. Department of Energy, Office of Science under DOE (BES) Award DE-SC0019165. Further support for this research was provided by the Office of the Vice Chancellor for Research and Graduate Education at the University of Wisconsin-Madison with funding from the Wisconsin Alumni Research Foundation.

Appendix A. Shale sample mineral composition

Table A.3 summarizes the mineral composition in weight percentage of the Wolfcamp sample used in the experiments.

Table A.3: Mineral composition of the Wolfcamp sample.

Mineral	Quartz	K-Feldspar	Plagioclase	Calcite	Dolomite	Pyrite	Marcasite	Illite Smectite Mica	Organic Matter
wt%	60.4	0.8	4.7	0.2	3.6	2.1	0.4	25.1	2.7

Appendix B. Concatenating multiple PET scans

Figure B.8 illustrates the PET scan concatenation and decay correction back to the beginning of the first scan. Our recent work verified that radioactivity is conserved across multiple scans after decay correction [38]. The uncorrected

(dashed line) in Figure B.8 also illustrates how the signal from the radiotracer decreases through time due to the radioactive decay of the 110 minute half-life ^{18}F radioisotope.

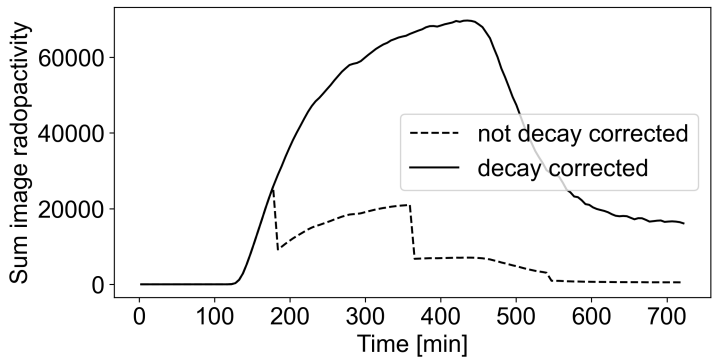

Figure B.8: Total activity in core as a function of time in PET scan prior to acidified brine injection.

Appendix C. Reactive transport results for non carbonate species

Table C.4 and C.5 show the aqueous reactions and mineral kinetic reactions respectively. Aqueous kinetic reactions respect a rate-dependent transition state theory (TST) rate law as shown in Equation C.1 [56] where $\prod$ $(\mathrm{a}_i)^n$ indicates the product of rate dependency on all aqueous species, K_{eq} refers to equilibrium constant, k is the reaction rate constant in mol(kg water)$^{-1}$yr^{-1}, and IAP is the ion activity product.

$$R = k \prod (a_i)^n [1 - \frac{\mathrm{IAP}}{K_{eq}}] \tag{C.1}$$

Mineral dissolution and precipitation also respect a TST rate law as shown in Equation C.2 [56] where $\prod$ $(\mathrm{a}_i)^n$ shows rate dependency on species a, K_{sp} refers to solubility product of the mineral, k is the rate constant in mol·m^{-2}s^{-1}, A_m is mineral surface area in m^{2}s^{-1}, and IAP is the ion activity product. Temperature dependence of the rate constants are accounted fo by the CrunchFlow

numerical simulator using the Arrhenius equation. A_m is set to one for pre-existing minerals and set to 0.1 for secondary minerals that may precipitate such as gypsum, halite, $Fe(OH)_3$, and amorphous SiO_2.

$$R = A_m k \prod (a_i)^n [1 - \frac{\text{IAP}}{K_{eq}}] \tag{C.2}$$

Table C.4: Instantaneous aqueous speciation reactions considered for the reactive transport model. The equilibrium constants are reported for 40°C and derived from Li et al [57].

Equilibrium Reactions [57]	$\log_{10}(K_{eq})$ [57]
$Fe^{3+} + 0.5H_2O \leftrightarrow Fe^{2+} + H^+ + 0.25O_2(aq)$	-7.66
$AlOH^{2+} + H^+ \leftrightarrow Al^{3+} + H_2O$	4.53
$Al(OH)_2^+ + 2H^+ \leftrightarrow Al^{3+}\ 2H_2O$	9.76
$Al(SO)_4^+ \leftrightarrow SO_4^{2-} + Al^{3+}$	-3.01
$MgCl^+ \leftrightarrow Cl^- + Mg^{2+}$	0.12
$H_2S(aq) \leftrightarrow H^+ + HS^-$	-6.81
$H_2SO_4(aq) \leftrightarrow 2H^+ + SO_4^{2-}$	1.02
$HSO_4^- \leftrightarrow H^+ + SO_4^{2-}$	-2.14
$CaCl^+ \leftrightarrow Ca^{2+} + Cl^-$	0.67
$CaCl_2(aq) \leftrightarrow Ca^{2+} + 2Cl^-$	0.67
$CaOH^+ + H^+ \leftrightarrow Ca^{2+} + H_2O$	12.9
$CaSO_4(aq) \leftrightarrow Ca^{2+} + SO_4^{2-}$	-2.16
$HCl(aq) \leftrightarrow H^+ + Cl^-$	-0.69
$H^+ + OH^- \leftrightarrow H_2O$	13.54
$CO_2(aq) + H_2O \leftrightarrow H^+ + HCO_3^-$	-6.28
$CO_3^{2-} + H^+ \leftrightarrow HCO_3^-$	10.22

Additional observations from the reactive transport model suggest volume reduction of K-feldspar, albite, pyrite, and smectite with time due to dissolution that occurs at a significantly lower rate than carbonates (Figure C.9). These plots show that the precipitation of pyrite is followed immediately after dissolution.

Table C.5: Mineral kinetic reactions and their model parameters. $\Pi(a_i)^n$ shows rate dependency on species a, $\log_{10}(K_{sp})$ is solubility product of minerals at 40°C and $\log_{10}(k)$ is the rate constant in mol·m^{-2}s^{-1} shown for 25°C.

Minerals	Reactions [57]	$\prod(a_i)^n$ [57]	$\log_{10}(K_{sp})$ [57]	$\log_{10}(k)$
Quartz	Quartz ↔ SiO_2(aq)	None	-3.74	-15[57]
K-Feldspar	K-Feldspar + $4H^+$ ↔ Al^{3+} + K^+ + $2H_2O$ + $3SiO_2$(aq)	None	-0.53	-11.5[58]
Albite	Albite + $4H^+$ ↔ Al^{3+} + Na^+ + $2H_2O$ + $3SiO_2$(aq)	None	2.27	-11.5[59, 60]
Calcite	Calcite + H^+ ↔ Ca^{2+} + HCO_3^-	$(H^+)^{1.0}$	1.63	-3.5[57]
Dolomite	Dolomite + $2H^+$ ↔ Ca^{2+} + Mg^{2+} + $2HCO_3^-$	$(H^+)^{0.5}$, None	2.0	-7.7[57]
Pyrite	Pyrite + H_2O ↔ Fe^{2+} + $1.75HS^-$ + $0.25SO_4^{2-}$ + $0.25H^+$	None	-23.75	-7.5[59, 61]
Illite	Illite + $8H^+$ ↔ $0.25Mg^{2+}$ + $0.6K^+$ + $2.3Al^{3+}$ $3.5SiO_2$(aq) + $5H_2O$	None	7.51	-11[57]
Smectite	Smectite + $7H^+$ ↔ $0.02Ca^{2+}$ + $0.15Na^+$ + $0.16Fe^{3+}$ + $0.2K^+$ + $0.29Fe^{3+}$ + $0.9Mg^{2+}$ + $1.25Al^{3+}$ + $3.75SiO_2$(aq)	None	8.53	-11[59, 62]
Gypsum	Gypsum ↔ Ca^{2+} + SO_4^{2-}	None	-4.51	-30[57]
Halite	Halite ↔ Na^+ + Cl^-	None	1 61	-0.21[59, 63]
$Fe(OH)_3$	$Fe(OH)_3$ + $3H^+$ ↔ Fe^{3+} + $3H_2O$	$(H^+)^{1.0}$	-5.30	-8.5[57]
SiO_2(am)	SiO_2(am) ↔ SiO_2(aq)	None	-2.56	-8[57]

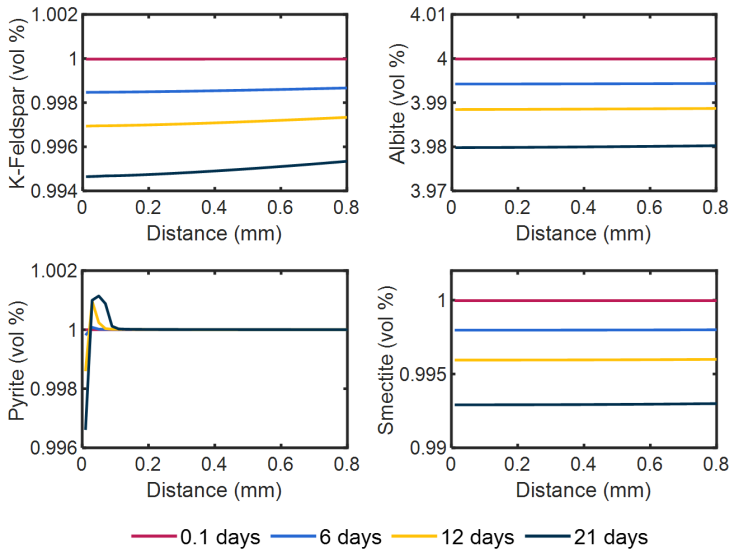

Figure C.9: Volume reductions of K-feldspar (upper left), albite (upper right), pyrite (lower left), and smectite (lower right) indicate slow dissolution of these minerals at the fracture-matrix interface.

References

[1] A. Vengosh, R. B. Jackson, N. Warner, T. H. Darrah, A. Kondash, A critical review of the risks to water resources from unconventional shale gas development and hydraulic fracturing in the United States, Environmental Science and Technology 48 (15) (2014) 8334–8348. doi:10.1021/es405118y.

[2] M. A. Ferno, L. P. Hauge, A. Uno Rognmo, J. Gauteplass, A. Graue, M. A. Fernø, L. P. Hauge, A. Uno Rognmo, J. Gauteplass, A. Graue, Flow visualization of CO2 in tight shale formations at reservoir conditions, Geophysical Research Letters 42 (18) (2015) 7414–7419. doi:10.1002/2015GL065100. URL `http://doi.wiley.com/10.1002/2015GL065100`

[3] C. Zahasky, S. Benson, Evaluation of hydraulic controls for leakage intervention in carbon storage reservoirs, International Journal of Greenhouse Gas Control 47 (2016) 86–100. doi:10.1016/j.ijggc.2016.01.035.

[4] Q. C. Wenning, C. Madonna, T. Kurotori, C. Petrini, J. Hwang, A. Zappone, S. Wiemer, D. Giardini, R. Pini, Chemo-Mechanical Coupling in Fractured Shale With Water and Hydrocarbon Flow, Geophysical Research Letters 48 (5) (2021) 0–12. doi:10.1029/2020GL091357.

[5] Q. Li, A. D. Jew, A. Kohli, K. Maher, G. E. Brown, J. R. Bargar, Thicknesses of Chemically Altered Zones in Shale Matrices Resulting from Interactions with Hydraulic Fracturing Fluid, Energy and Fuels 33 (8) (2019) 6878–6889. doi:10.1021/acs.energyfuels.8b04527.

[6] H. J. Khan, E. Spielman-Sun, A. D. Jew, J. Bargar, A. Kovscek, J. L. Druhan, A Critical Review of the Physicochemical Impacts of Water Chemistry on Shale in Hydraulic Fracturing Systems, Environmental Science and Technology 55 (3) (2021) 1377–1394. doi:10.1021/acs.est.0c04901.

[7] B. F. Esteves, E. Spielman-Sun, Q. Li, A. D. Jew, J. R. Bargar, J. L. Druhan, Geochemical modeling of celestite (srso4) precipitation and reactive transport in shales, Environmental Science & Technology 56 (7) (2022) 4336–4344.

[8] D. Sassani, C. Stone, F. Hansen, E. Hardin, T. Dewers, M. Martinez, R. Rechard, S. Sobolik, G. Freeze, R. Cygan, K. Gaither, J. Holland, P. Brady, Shale disposal of U.S. high-level radioactive waste., Tech. Rep. May, Sandia National Laboratories (SNL), Albuquerque, NM, and Livermore, CA (United States) (may 2010). doi:10.2172/992338.
URL `https://www.osti.gov/servlets/purl/992338/`

[9] L. F. Orellana, C. Giorgetti, M. Violay, Contrasting mechanical and hydraulic properties of wet and dry fault zones in a proposed shale-hosted nuclear waste repository, Geophysical Research Letters 46 (3) (2019) 1357–1366. arXiv:https://agupubs.onlinelibrary.wiley.com/doi/pdf/10.1029/2018GL080384, doi:https://doi.org/10.1029/2018GL080384.
URL `https://agupubs.onlinelibrary.wiley.com/doi/abs/10.1029/2018GL080384`

[10] J. Warren, P. Root, The Behavior of Naturally Fractured Reservoirs, Society of Petroleum Engineers Journal 3 (03) (1963) 245–255. doi:10.2118/426-pa.

[11] K. Pruess, T. N. Narasimhan, A Practical Method for Modeling Fluid and Heat Flow in Fractured Porous Media, Society of Petroleum Engineers Journal 25 (01) (1985) 14–26. arXiv:https://onepetro.org/spejournal/article-pdf/25/01/14/2647668/spe-10509-pa.pdf, doi:10.2118/10509-PA.
URL `https://doi.org/10.2118/10509-PA`

[12] H. H. Gerke, M. van Genuchten, Dual porosity model for simulating the prefrential movement of water and solutes in structured porous media, Water Resources Research 29 (2) (1993) 305–319.

[13] B. W. Arnold, H. Zhang, A. M. Parsons, Effective-porosity and dual-porosity approaches to solute transport in the saturated zone at yucca mountain: Implications for repository performance assessment, Geophysical Monograph Series 122 (2000) 313–322. doi:10.1029/GM122p0313.

[14] J. D. Hyman, S. Karra, N. Makedonska, C. W. Gable, S. L. Painter, H. S. Viswanathan, DfnWorks: A discrete fracture network framework for modeling subsurface flow and transport, Computers and Geosciences 84 (2015) 10–19. doi:10.1016/j.cageo.2015.08.001.
URL `http://dx.doi.org/10.1016/j.cageo.2015.08.001`

[15] C. R. Romano, R. T. Williams, Evolution of Fault-Zone Hydromechanical Properties in Response to Different Cementation Processes, Lithosphere 2022 (1) (2022). doi:10.2113/2022/1069843.

[16] M. B. Cardenas, D. T. Slottke, R. A. Ketcham, J. M. S. Jr, Navier-Stokes flow and transport simulations using real fractures shows heavy tailing due to eddies, Geophysical Research Letters 34 (July) (2007) 1–6. doi:10.1029/2007GL030545.

[17] S. Yoon, P. K. Kang, Roughness, inertia, and diffusion effects on anomalous transport in rough channel flows, Physical Review Fluids 6 (1) (2021) 14502. doi:10.1103/PhysRevFluids.6.014502.
URL https://doi.org/10.1103/PhysRevFluids.6.014502

[18] C. Soulaine, P. Creux, H. A. Tchelepi, Micro-continuum Framework for Pore-Scale Multiphase Fluid Transport in Shale Formations, Transport in Porous Media 127 (1) (2019) 85–112. doi:10.1007/s11242-018-1181-4.
URL https://doi.org/10.1007/s11242-018-1181-4

[19] I. Neretnieks, Diffusion in the rock matrix: An important factor in radionuclide retardation?, Journal of Geophysical Research 85 (B8) (1980) 4379. doi:10.1029/JB085iB08p04379.

[20] M. T. V. Genuchten, W. J. Alves, Analytical Solutions of the 1D Convective-Dispersive Solute Transport Equation, Tech. Rep. 1661, U.S. Department of Agriculture, Beltsville, MD (1982).

[21] D. H. Tang, E. O. Frind, E. A. Sudicky, Contaminant transport in fractured porous media: Analytical solution for a single fracture, Water Resources Research 17 (3) (1981) 555–564. doi:10.1029/WR017i003p00555.
URL http://doi.wiley.com/10.1029/WR017i003p00555

[22] D. Roubinet, J. R. De Dreuzy, D. M. Tartakovsky, Semi-analytical solutions for solute transport and exchange in fractured porous media, Water Resources Research 48 (1) (2012) 1–10. doi:10.1029/2011WR011168.

[23] A. D. Jew, J. L. Druhan, M. Ihme, A. R. Kovscek, I. Battiato, J. P. Kaszuba, J. R. Bargar, G. E. Brown Jr, Chemical and reactive transport processes associated with hydraulic fracturing of unconventional oil/gas shales, Chemical reviews 122 (9) (2022) 9198–9263.

[24] C. I. Steefel, K. T. MacQuarrie, Approaches to modeling of reactive transport in porous media, Reactive transport in porous media (2018) 83–130.

[25] J. M. Galíndez, J. Molinero, Assessment of the long-term stability of cementitious barriers of radioactive waste repositories by using digital-image-based microstructure generation and reactive transport modelling, Cement and Concrete Research 40 (8) (2010) 1278–1289.

[26] M. Xie, K. U. Mayer, F. Claret, P. Alt-Epping, D. Jacques, C. Steefel, C. Chiaberge, J. Simunek, Implementation and evaluation of permeability-porosity and tortuosity-porosity relationships linked to mineral dissolution-precipitation, Computational Geosciences 19 (3) (2015) 655–671.

[27] K. T. MacQuarrie, K. U. Mayer, Reactive transport modeling in fractured rock: A state-of-the-science review, Earth Science Reviews 72 (3-4) (2005) 189–227.

[28] C. I. Steefel, D. J. DePaolo, P. C. Lichtner, Earth and planetary science letters, Reactive transport in porous media (3-4) (2005) 539–558.

[29] C. Steefel, C. Appelo, B. Arora, D. Jacques, T. Kalbacher, O. Kolditz, V. Lagneau, P. Lichtner, K. U. Mayer, J. Meeussen, et al., Reactive transport codes for subsurface environmental simulation, Computational Geosciences 19 (3) (2015) 445–478.

[30] J. Druhan, C. Tournassat, M. S. of Mineralogical Society of America, Reactive transport in natural and engineered systems, Vol. 85, Mineralogical Society of America, 2019.

[31] H. J. Khan, C. M. Ross, J. L. Druhan, Impact of concurrent solubilization and fines migration on fracture aperture growth in shales during acidized brine injection, Energy & Fuels 36 (11) (2022) 5681–5694. doi:https://doi.org/10.1021/acs.energyfuels.2c00611.
URL https://pubs.acs.org/doi/full/10.1021/acs.energyfuels.2c00611

[32] M. H. Bradbury, A. Green, Measurement of important parameters determining aqueous phase diffusion rates through crystalline rock ma-

trices, Journal of Hydrology 82 (1-2) (1985) 39–55. doi:10.1016/0022-1694(85)90045-9.

[33] K. Skagius, I. Neretnieks, Diffusivity Measurements and Electrical Resistivity Measurements in Rock Samples Under Mechanical Stress, Water Resources Research 22 (4) (1986) 570–580. doi:10.1029/WR022i004p00570. URL http://doi.wiley.com/10.1029/WR022i004p00570

[34] A. S. Grader, M. Balzarini, F. Radaelli, G. Capasso, A. Pellegrino, Fracture-matrix flow: Quantification and visualization using X-Ray computerized tomography, 2000, pp. 157–168. doi:10.1029/GM122p0157. URL http://www.agu.org/books/gm/v122/GM122p0157/GM122p0157.shtml

[35] S. Akin, A. Kovscek, Computed Tomography in Petroleum Engineering Research, Applications of X-ray Computed Tomography in the Geosciences 215 (2003) 23–38.

[36] C. Zahasky, D. Thomas, J. Matter, K. Maher, S. M. Benson, Multimodal imaging and stochastic percolation simulation for improved quantification of effective porosity and surface area in vesicular basalt, Advances in Water Resources 121 (June) (2018) 235–244. doi:10.1016/j.advwatres.2018.08.009. URL https://doi.org/10.1016/j.advwatres.2018.08.009

[37] C. Zahasky, T. Kurotori, R. Pini, S. M. Benson, Positron emission tomography in water resources and subsurface energy resources engineering research, Advances in Water Resources 127 (March) (2019) 39–52. doi:10.1016/j.advwatres.2019.03.003. URL https://doi.org/10.1016/j.advwatres.2019.03.003

[38] T. Kurotori, C. Zahasky, M. Gran, A. R. Kovscek, S. M. Benson, Comparative analysis of imaging and measurements of micrometer-scale fracture aperture fields within a heterogeneous rock using PET and X-ray CT (In Review).

[39] C. Zahasky, S. M. Benson, Micro-Positron Emission Tomography for Measuring Sub-core Scale Single and Multiphase Transport Parameters in Porous Media, Advances in Water Resources 115 (2018) 1–16. doi:10.1016/j.advwatres.2018.03.002.
URL http://linkinghub.elsevier.com/retrieve/pii/S030917081731182X

[40] C. R. Romano, C. Zahasky, C. Garing, J. M. Minto, S. M. Benson, Z. K. Shipton, R. J. Lunn, Sub-core scale fluid flow behavior in a sandstone with cataclastic deformation bands, Water Resources Research (2020) 1–16doi:10.1029/2019wr026715.

[41] C. Zahasky, S. M. Benson, Preferential Solute Transport in Low Permeability Zones During Spontaneous Imbibition in Heterogeneous Porous Media, Water Resources Research 58 (1) (2022). doi:10.1029/2020wr029460.

[42] T. Kurotori, C. Zahasky, S. Hosseinzadeh Hejazi, S. Shah, S. Benson, R. Pini, Measuring, imaging and modelling solute transport in a microporous limestone, Chemical Engineering Science 196 (2019). doi:10.1016/j.ces.2018.11.001.

[43] T. Kurotori, M. P. Murugesu, C. Zahasky, B. Vega, J. L. Druhan, S. M. Benson, A. R. Kovscek, Mixed Imbibition Controls The Advance of Wetting Fluid in Multiscale Geological Media (In Review).

[44] R. Pini, S. C. Krevor, S. M. Benson, Capillary pressure and heterogeneity for the CO2/water system in sandstone rocks at reservoir conditions, Advances in Water Resources 38 (2012) 48–59. doi:10.1016/j.advwatres.2011.12.007.
URL http://linkinghub.elsevier.com/retrieve/pii/S0309170811002363

[45] A. S. Gundogar, C. M. Ross, A. D. Jew, J. R. Bargar, A. R. Kovscek, Multiphysics investigation of geochemical alterations in marcellus shale using reactive core-floods, Energy & Fuels 35 (13) (2021) 10733–10745. doi:https://doi.org/10.1021/acs.energyfuels.1c00588.
URL https://pubs.acs.org/doi/10.1021/acs.energyfuels.1c00588

[46] A. F. Frangi, W. J. Niessen, K. L. Vincken, M. A. Viergever, Multiscale vessel enhancement filtering, in: W. M. Wells, A. Colchester, S. Delp (Eds.), Medical Image Computing and Computer-Assisted Intervention — MICCAI'98, Springer Berlin Heidelberg, Berlin, Heidelberg, 1998, pp. 130–137.

[47] L. Li, L. Zhu, C. Ma, L. Lin, J. Yao, L. Wang, K. Maslov, R. Zhang, W. Chen, J. Shi, L. V. Wang, Single-impulse panoramic photoacoustic computed tomography of small-animal whole-body dynamics at high spatiotemporal resolution, Nature Biomedical Engineering 1 (5) (2017) 0071. doi:10.1038/s41551-017-0071.
URL `http://www.nature.com/articles/s41551-017-0071`

[48] Y. Liu, L. Peng, S. Huang, X. Wang, Y. Wang, Z. Peng, River detection in high-resolution sar data using the frangi filter and shearlet features, Remote Sensing Letters 10 (10) (2019) 949–958. arXiv:https://doi.org/10.1080/2150704X.2019.1635286, doi:10.1080/2150704X.2019.1635286.
URL `https://doi.org/10.1080/2150704X.2019.1635286`

[49] J. Bear, Dynamics of Fluids in Porous Media, Dover Publications, Inc, New York, 1972.

[50] S. Li, Z. Li, Q. Dong, Diffusion coefficients of supercritical CO2 in oil-saturated cores under low permeability reservoir conditions, Journal of CO2 Utilization 14 (2016) 47–60. doi:10.1016/j.jcou.2016.02.002.
URL `http://dx.doi.org/10.1016/j.jcou.2016.02.002`

[51] R. R. Ratnakar, B. Dindoruk, The Role of Diffusivity in Oil and Gas Industries: Fundamentals, Measurement, and Correlative Techniques, Processes 10 (6) (2022) 1194. doi:10.3390/pr10061194.
URL `https://www.mdpi.com/2227-9717/10/6/1194`

[52] N. A. Mumallah, Hydrochloric acid diffusion coefficients at acid-fracturing conditions, Journal of Petroleum Science and Engineering 15 (2) (1996)

361–374. doi:https://doi.org/10.1016/0920-4105(95)00086-0.
URL https://www.sciencedirect.com/science/article/pii/0920410595000860

[53] C. Noiriel, B. Madé, P. Gouze, Impact of coating development on the hydraulic and transport properties in argillaceous limestone fracture, Water Resources Research 43 (9) (2007). arXiv:https://agupubs.onlinelibrary.wiley.com/doi/pdf/10.1029/2006WR005379, doi:https://doi.org/10.1029/2006WR005379.
URL https://agupubs.onlinelibrary.wiley.com/doi/abs/10.1029/2006WR005379

[54] J. Du, L. Hu, J. N. Meegoda, G. Zhang, Shale softening: Observations, phenomenological behavior, and mechanisms, Applied Clay Science 161 (2018) 290–300. doi:https://doi.org/10.1016/j.clay.2018.04.033.
URL https://www.sciencedirect.com/science/article/pii/S0169131718301935

[55] C. Zahasky, M. Murugesu, T. Kurotori, C. Sutton, J. Druhan, B. Vega, S. M. Benson, A. Kovscek, Solute transport maps in a naturally fractured shale rock before and after acidified brine injection - 4D imaging dataset and analytical model (2023). doi:https://doi.org/10.25740/pv902jr5822.

[56] C. I. Steefel, S. Molins, Crunchflow, Software for modeling multicomponent reactive flow and transport. User's manual. Lawrence Berkeley National Laboratory, Berkeley (2009).

[57] Q. Li, A. D. Jew, G. E. Brown Jr, J. R. Bargar, K. Maher, Reactive transport modeling of shale–fluid interactions after imbibition of fracturing fluids, Energy & Fuels 34 (5) (2020) 5511–5523.

[58] H. C. Helgeson, W. M. Murphy, P. Aagaard, Thermodynamic and kinetic constraints on reaction rates among minerals and aqueous solutions. ii. rate constants, effective surface area, and the hydrolysis of feldspar, Geochimica et Cosmochimica Acta 48 (12) (1984) 2405–2432.

[59] J. L. Palandri, Y. K. Kharaka, A compilation of rate parameters of water-mineral interaction kinetics for application to geochemical modeling, Tech.

rep., Geological Survey Menlo Park CA, Menlo Park, CA (United States) (2004).

[60] L. Chou, R. Wollast, Steady-state kinetics and dissolution mechanisms of albite, American Journal of Science 285 (10) (1985) 963–993.

[61] M. A. McKibben, H. L. Barnes, Oxidation of pyrite in low temperature acidic solutions: Rate laws and surface textures, Geochimica et Cosmochimica Acta 50 (7) (1986) 1509–1520.

[62] A. Bauer, G. Berger, Kaolinite and smectite dissolution rate in high molar koh solutions at 35 and 80 c 13 (7) (1998) 905–916.

[63] M. Alkattan, E. H. Oelkers, J.-L. Dandurand, J. Schott, Experimental studies of halite dissolution kinetics, 1 the effect of saturation state and the presence of trace metals, Chemical Geology 137 (3-4) (1997) 201–219.